Energy Storage Materials 72 (2024) 103763

Contents lists available at ScienceDirect

Energy Storage Materials

journal homepage: www.elsevier.com/locate/ensm

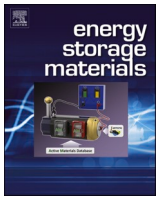

Mitigating Jahn–Teller effect of MnO_2 via charge regulation of Mn-local environment for advanced calcium storage

Chunli Zuo [a,e], Fangyu Xiong [b], Yihan Shao [a], Ming Li [c], Dongyao Zhu [d], Jiexin Zhu [a], John Wang [e,*], Qinyou An [a,f,*]

[a] State Key Laboratory of Advanced Technology for Materials Synthesis and Processing, Wuhan University of Technology, Wuhan 430070, China
[b] College of Materials Science and Engineering, Chongqing University, Chongqing, 400030, China
[c] School of Materials and Energy, University of Electronic Science and Technology of China, Chengdu 611731, China
[d] Hubei Provincial Key Laboratory of Green Materials for Light Industry School of Materials and Chemical Engineering, Hubei University of Technology, Wuhan 430068, China
[e] Department of Materials Science and Engineering, National University of Singapore, 117574, Singapore
[f] Hubei Longzhong Laboratory, Wuhan University of Technology (Xiangyang Demonstration Zone), Xiangyang 441000, China

ARTICLE INFO

Keywords:
Rechargeable Ca-ion batteries
MnO_2 cathode materials
Mn-local environment regulation
Mo doping
Jahn-Teller effect inhibition

ABSTRACT

Manganese dioxide (MnO_2) stands out as a prospective cathode material for calcium ion batteries (CIBs) owing to its elevated theoretical capacity and high operating voltage. Nevertheless, MnO_2 with Jahn-Teller (J-T) twisted MnO_6 octahedra experiences severe Mn dissolution during cycling, leading to the destabilization of the transition metal layer and resulting in poor cycling performance. In this work, Mo-substitution is purposely proposed to suppress the J-T effect in MnO_2 for CIBs. The local charge of Mn is regulated by Mo doping, which enhances the electrical conductivity of MnO_2 and suppresses the J-T distortion of the MnO_6 octahedron. Meanwhile, density-functional theory (DFT) calculations manifest that Mo doping enhances the structural integrity of MnO_2, making it difficult for Mn to escape from the MnO_6 structure and inhibiting the dissolution of Mn. Accordingly, Mo-MnO_2 demonstrates impressive rate capability (112 mAh g^{-1} at 1 A g^{-1}) and excellent cycling stability, maintaining approximately 93.9 % capacity after 900 cycles at 1 A g^{-1}. As a result, the introduction of heteroatoms through doping offers a novel design approach for the advancement of cathode materials for advanced CIBs.

1. Introduction

With the ever-rising demand for clean energy globally, renewable energy generation and storage technologies have become a hot topic of research and development [1–3]. In recent times, calcium ion batteries (CIBs) have garnered extensive interest owing to their cost-effectiveness, enhanced safety features, and the lower standard electrode potential of Ca (-2.87 V vs SHE) [4–6]. Additionally, the potentially high energy density of CIBs allows them a promising options for the next-generation battery technologies [7]. However, CIBs are still in the nascent phases of development and face several technical challenges, such as the slow ions migration kinetics during the reviserabile (de)insertion processes due to the larger radius of Ca ions [8]. Therefore, exploring high-performance cathode materials for CIBs has become a key focus of current research in new battery technologies.

In recent years, manganese dioxide (MnO_2) has garnered considerable interest owing to its benefits, including cost-effectiveness, adjustable valence, varied tunnel structure, substan-tial theoretical capacity (308 mAh g^{-1}) and high working voltage [9,10]. However, the overall performance is far from satisfactory in terms of Ca storage due to its inherent low electronic conductivity and structural instability (Jahn--Teller (J-T) aberration of Mn^{3+} cations) [11]. In addition, the large radius of Ca ions and the robust electrostatic interaction between Ca ions and Mn-oxygen layer result in the slow diffusion kinetics [12] (Fig. 1a). In order to solve this series of problems, ions with large radius have been introduced into the interlayer of MnO_2 aiming to improve the ion diffusion kinetics by expanding the layer spacing [13–17]. However, during the cycling process, the pre-intercalated ions/molecules are inevitably extracted from the interlayers into the electrolyte and there is insufficient inhibition of MnO_6 structure distortion. Ion doping is

* Corresponding authors at: State Key Laboratory of Advanced Technology for Materials Synthesis and Processing, Wuhan University of Technology, Wuhan 430070, China.
E-mail addresses: msewangj@nus.edu.sg (J. Wang), anqinyou86@whut.edu.cn (Q. An).

https://doi.org/10.1016/j.ensm.2024.103763
Received 21 July 2024; Received in revised form 22 August 2024; Accepted 1 September 2024
Available online 2 September 2024

recognized as one of the effective ways to alleviate the J-T effect [18,19]. The ion doping can modulate the electronic structure [20], enhance local electric fields [21–23], and balance charge distribution [24,25], thereby improving the ions/electron migration rate and structural stability of the cathode material. In recent years, Mo doping has been extensively studied in various battery systems. For example, Mo doping in $LiFePO_4$ has been shown to improve electrical conductivity and enhance cycling stability of lithium-ion batteries [26]. In zinc-ion batteries, pre-intercalation of Mo dopants as interlayer pillars not only expands the interlayer spacing but also reinforces the layered structure of δ-MnO_2 [27]. Nevertheless, there is little research work of done in doping MnO_2 as a cathode material for CIBs. Building on this, the present study investigates the effects of Mo doping on MnO_2 cathode materials, with a particular focus on its impact on capacity, rate performance, and overall electrochemical stability. Additionally, this study aims to further elucidate the role of Mo doping in these enhancements.

In the present work, Mo-doped manganese dioxide (MMO) was synthesized for the first time to regulate the CIBs. Mo was chosen as a dopant because of its abundant stabilizing valence states, which can regulate the local charge of Mn and stabilize the structural stability of MnO_2. In addition, the atomic radius of Mo is very close to that of the Mn, therefore it is expected to enter the MnO_2 crystals lattices [23]. Indeed, the characterization techniques indicate that the Mo is successfully introduced into the MnO_2 lattice and occupies the Mn positions, triggering a redistribution of local charges around in Mn. Furthermore, The characterization results from X-ray absorption fine structure (XAFS) and electron paramagnetic resonance (EPR) spectroscopy analysis, along with density functional theory (DFT) analysis, indicating that Mo doping enhances the local charge of Mn, reduces the band gap, thereby improving the intrinsic conductivity and activity of MnO_2. In addition, Mo-substituted doping can change the local structure and charge compensation mechanism of Mn, alleviate the Mn-O bond distortion, and improve the structural stability, leading to significant improvement in the long-cycle stability of MnO_2 (Fig. 1b). Currently, the main cathode materials for CIBs include NASICON-type, manganese-based, and vanadium-based materials. Manganese dioxide stands out as one of the most promising options for energy storage systems due to its non-polluting nature, high voltage and capacity, low cost, and abundant availability (Fig. 1c and **Table S1**) [12,28–37]. Benefiting from the raised electrical conductivity, the as-prepared Mo-MnO_2 (MMO) demonstrates a notable capacity of 142 mAh g^{-1} at 0.1 A g^{-1} and a significant long-term cycling stability. Both in-situ X-ray diffraction (XRD) and time-of-flight secondary-ion mass spectrometry (TOF-SIMS) demonstrate a reversible (de)intercalation mechanism of Ca ions in the MMO electrode.

2. Results and discussion

The MMO materials were synthesized via an one-step hydrothermal approach. Scanning electron microscopy (SEM) image (Fig. 2a) displays that MMO-40 has a flower-like morphology consisting of uniform nanosheets folding onto each other, where the average size of nanosheets is about 50–100 nm. Besides, the SEM images of pristine MnO_2 and MMO-20, 40, 60, 80 (**Figure S1a–e**) display that Mo doping did not change the flower-like morphology. The high-resolution transmission electron microscopy (HRTEM) images in Fig. 2b and **S2** indicate that a subtle enlargement in the interlayer spacing from 0.70 nm to 0.72 nm after Mo doping. This implies that the substitutional doping of Mo leads to a minor expansion of the manganese oxide layers. The TEM images, along with the corresponding energy dispersive spectroscopy (EDS) mapping, illustrating the uniform distribution of Mn, O, and Mo elements within the MMO-40 sample (Fig. 2c). The local structure of MMO-40 was further probed by X-ray scattering. Fourier transform and Lorch

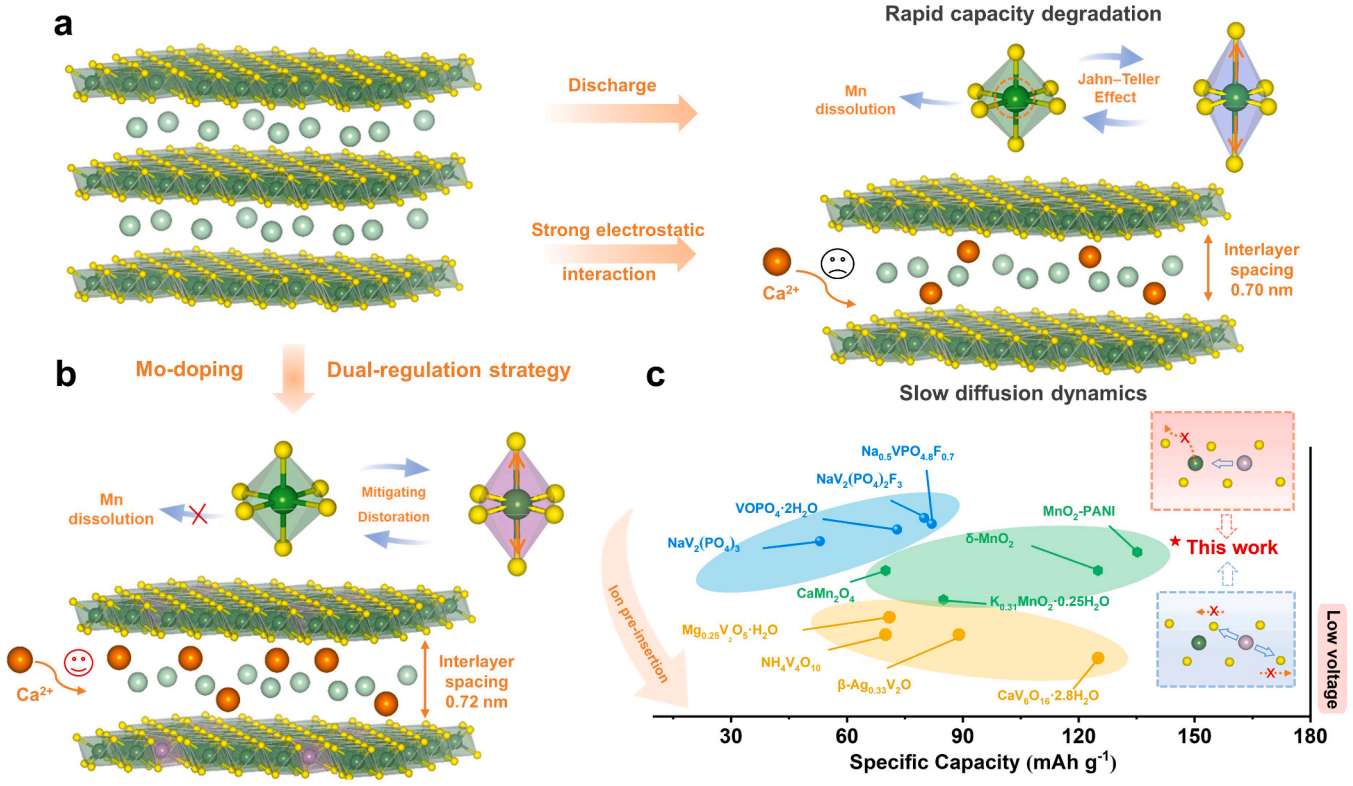

Fig. 1. Schematic illustration of the Mo-doped strategy. (a) The pristine MnO_2 suffers from severe dissolution of Mn^{2+} due to the disproportionation reaction of Mn^{3+} and the strong electrostatic interaction between Ca^{2+} ions and host material results in slow diffusion dynamics. (b) Mo-doped design effectively promotes ion diffusion and suppresses the J-T effect. (c) The ragone plots of average output voltage versus specific capacity for MMO-40 and some state-of-the-art cathode materials for CIBs.

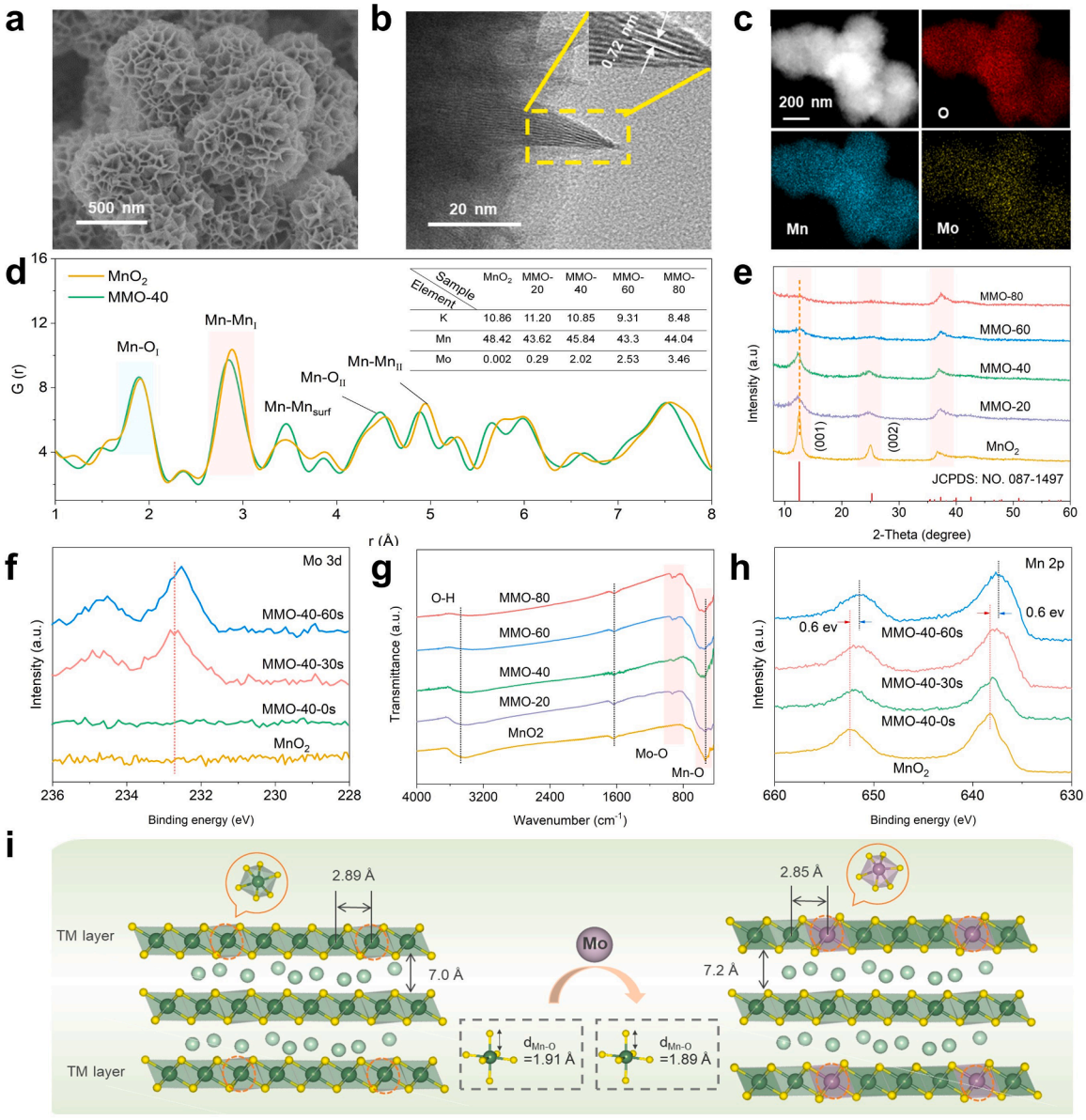

Fig. 2. (a) SEM image of MMO-40. (b) HRTEM image of MMO-40. (c) TEM-EDS mapping of MMO-40. (d) PDF analysis of the MnO_2 and MMO-40. (e) XRD patterns of pristine MnO_2 and MMO-20, 40, 60, 80. (f) Mo 3d XPS results at 0, 30 and 60s. (g) FTIR spectra of pristine MnO_2 and MMO-20, 40, 60, 80. (h) Mn 2p XPS results at 0, 30 and 60s. (i) Schematic synthesis of the MMO-40.

modification were applied to the faber-ziman total structure factor S(Q) to obtain the PDF, G(r), providing information on the distance between atomic pairs [38]. The G(r) plot of MMO-40 is similar to that of MnO_2 (Fig. 2d), suggesting that the crystal structure change of MnO_2 is slight after the introduction of Mo. Besides, the peak of Mn—O bonds shifts to lower pair distances after Mo doping, which can be attributed to lattice parameter contraction due to the partial reduction of Mn [39]. The peak at 2.89 Å corresponding to the Mn-Mn bond exhibits lower intensity after Mo doping, confirming that the partial substitution of Mn atoms by Mo atoms leads to the reduction of the Mn—Mn bond [40]. To investigate the influence of the Mo doping amount in the MnO_2 structure, the quantity of ammonium molybdate was varied within the range of 20 mg to 80 mg (MMO-20, 40, 60, 80). In the XRD patterns of the pristine MnO_2 and MMO-20, 40, 60, 80 samples (Fig. 2e), all characteristic peaks correspond well to those of birnessite (δ-MnO_2) (JCPDS No. 80-1098) [41]. As the doping amount of Mo increases, the diffraction peak of the (001) plane gradually weakens and shifts towards lower angle, indicating that the interlayer spacing is expanded by the Mo doping. Notably, excessive Mo doping leads to an amorphous structure [42]. In addition, The XRD pattern of MMO reveals no signs of impurities, indicating that Mo ions have entered into the MnO_2 crystal lattice. To explore the Mo distribution in the MMO-40 sample, X-ray photoelectron spectroscopy (XPS) etching experiments were conducted (Fig. 2f). The intensity of Mo increases with etching time, which indicates that Mo is distributed inside the particles rather than being enriched on the particle surface [43]. Additionally, the fitting of Mo 3d XPS spectrum indicates that the valence state of Mo in MMO-40 is +6 (**Figure S3**). In the fourier transform infrared spectrometer (FTIR) spectra of MnO_2 and MMO-40 (Fig. 2g), the peak at 529 cm^{-1} corresponds to the Mn-O vibration of MnO_6 octahedra. The considerable blue shift of this peak indicates that Mo doping enhances the strength of the Mn-O bond [44], thereby improving the stability of the manganese oxide layer [45,46]. The MMO-40 exhibits a new characteristic peak at 933 cm^{-1}, attributed to the formation of Mo-O bond resulting from the substitution of Mo for Mn [47]. In the Raman spectrum of MMO-40, the Mn-O bond peak shifts toward lower angles and exhibits reduced intensity, which is due to the

sturctural disordering arising from Mo doping (**Figure S4**) [48,49]. The electronic structure of MMO-40 was analyzed using XPS (Fig. 2h). The binding energy of Mn $2p_{3/2}$ and Mn $2p_{1/2}$ in MMO-40 are negatively shifted by about 0.6 eV compared to pristine MnO_2, which demonstrate that the eletrons migrated from the Mo dopant to MnO_2 [48,50]. To further determine the position of Mo in the crystal structure, the DFT calculations were conducted to investigate two possible structural models, including Mo at Mn site and interlayered site (**Figure S5**). In the case of perfect crystal MnO_2, the Mo preferentially occupied interlayer site with a formation energy ΔE of −1.97 eV, which is significantly lower than that of Mo occupied Mn site (0.071 eV). In the presence of manganese vacancy, the Mo preferentially occupied Mn vacancy with a formation energy ΔE of −6.97 eV, significantly lower than that of occupied interlayer site (−3.351 eV). There are a considerable number of Mn vacancies in δ-MnO_2 synthesized under acidic conditions [51,52]. Therefore, the above results indcate that the Mo has been introduced to replace the Mn site. According to the pair distribution function (PDF) test, slight alterations were observed in the bond lengths of the Mn-O bonds and the layer spacing of the Mn-O layers after Mo doping, as depicted in Fig. 2i. Finally, the chemical formula of MMO-40 and MnO_2 were determined as $K_{0.3}(Mo_{0.04}Mn_{0.96})O_2{\cdot}0.25H_2O$ and $K_{0.32}MnO_2{\cdot}0.23H_2O$, respectively, based on thermogravimetric analysis (TGA) and inductively coupled plasma (ICP) (**Figure S6** and **Table S2**).

To examine the Ca ions storage performance of the synthesized materials, we fabricated swagelock-type batteries (as illustrated in **Figure S7a**) and CR2016 coin cells for electrochemical assessments. In the swagelock-type battery, MMO-40 served as the working electrode, while activated carbon cloth (AC) served as the counter electrode, with Ag/AgCl reference electrode and $Ca(TFSI)_2$ dissolved in acetonitrile as electrolyte (**Figure S7b**). The cyclic voltammetry (CV) measurement is conducted with a scan rate of 0.2 mV s^{-1} (**Figure S8**). In the initial scan, a pair of cathodic/anodic peak appeared at around 3.44 V and 2.11 V (vs Ca^{2+}/ Ca). The CV curve show a symmetric intercalation and deintercalation of Ca ions. In addition, to facilitate the test of the electrochemical performance of the MMO-40 cothade material, the CR2016 cion cells were conducted. As depicted in Fig. 3a, the CV curve of MMO-40 shows a pair of reversible reduction peaks (at 3.44 V and 2.12 V) corresponding to the reversible insertion/extraction of Ca ions. This consistency in redox reaction potentials is observed across various systems. The CV curves of MMO-40 and MnO_2 electrodes are similar, indicating that these two samples undergo the similar oxidation/reduction process. It is noteworthy that the peak current of the MMO-40 electrode is higher than that of the MnO_2 electrode, confirming the enhancement of electrochemical activity and electrode reaction kinetics

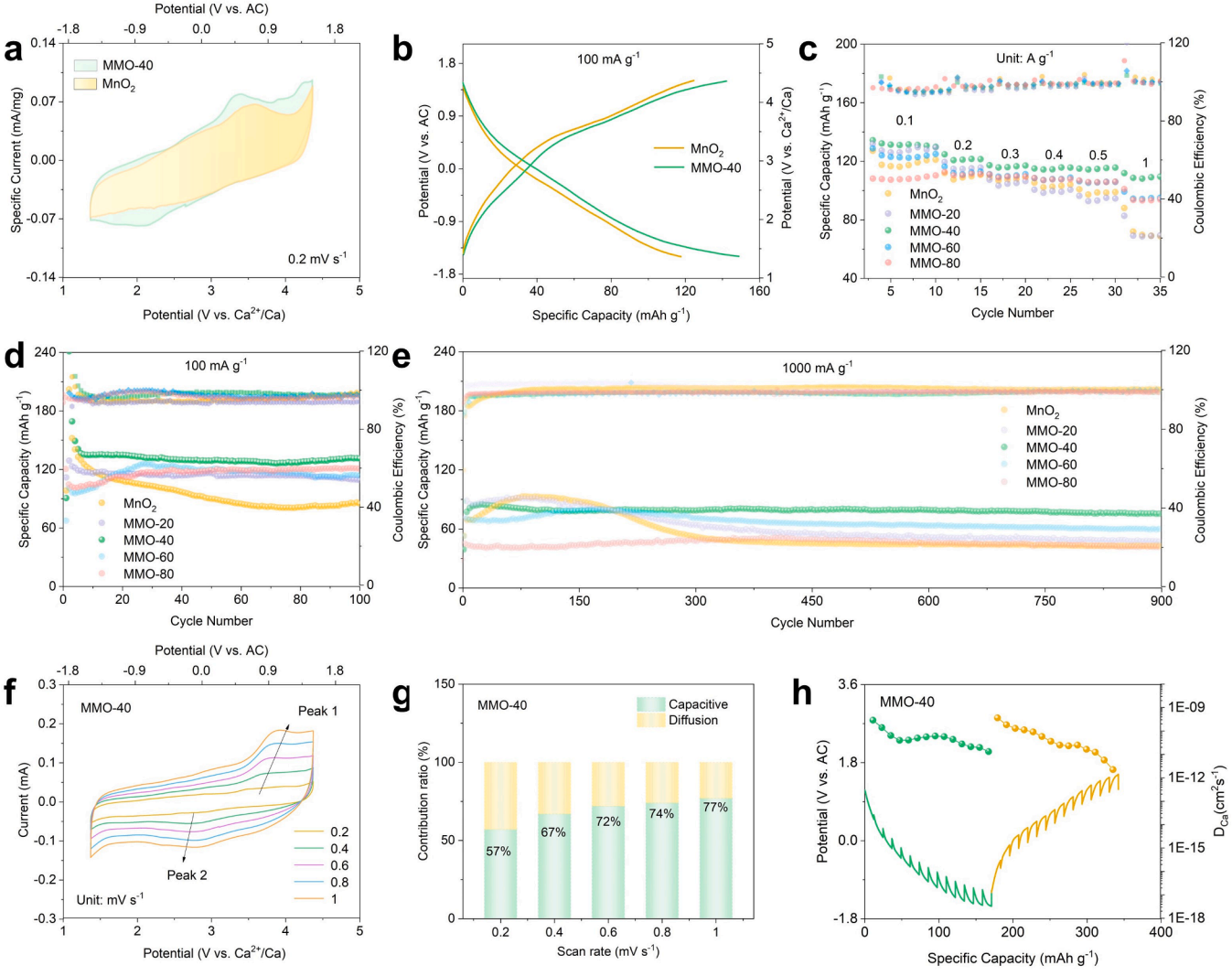

Fig. 3. (a) CV curves of MnO_2 and MMO-40. (b) Corresponding GCD profiles of MnO_2 and MMO-40 at 0.1 A g^{-1}. (c,d) Cycling performance and rate performance of MnO_2 and MMO-20, 40, 60, 80. (e) Cycling performance of MnO_2 and MMO-20, 40, 60, 80 at 1.0 A g^{-1}. (f) CV curves at various scan rate from 0.2 to 1.0 mV s^{-1}. (g) The contribution ratios of the capacitive capacities in MMO-40 electrode. (h) Discharge-charge GITT profiles and the corresponding Ca ions diffusion coefficient of MMO-40 cathode.

after Mo doping. The CV curves of MMO-40 exhibit good overlap in the first three cycles, indicating the good reversibility of electrochemical reaction (**Figure S9**). Furthermore, the galvanostatic charge-discharge (GCD) curves (Fig. 3b) indicate that MMO-40 exhibits a lower polarization potential and higher specific capacity compared to those of MnO_2. The rate performance and the cycling stability were investigated for MnO_2 and MMO-20, 40, 60, 80 (Fig. 3c and d). The specific capacity of MMO-40 retains 140, 124, 117,115, 114 and 112 mAh g^{-1} at the current densities of 0.1, 0.2, 0.3, 0.4, 0.5, and 1 A g^{-1}, respectively. Evidently, MMO-40 demonstrates superior performance in terms of both specific capacity and capacity retention, achieving an outstanding capacity retention of 96 % (135 mAh g^{-1}) at 0.1 A g^{-1}. Additionally, the GCD curves show little change in the polarization of MMO-40 with increasing current density (**Figure S10**). Under the condition of 1 A g^{-1}, MMO-40 shows the most robust long-term cycling performance, maintaining a capacity retention rate of 93.9 % after 900 cycles (Fig. 3e). The excellent cycle stability (**Figure S11**) of MMO-40 cathode is superior to that of previously reported other CIBs cathode materials (**Table S3**). To illustrate the significant potential of MMO-40, a Ca-metal cell was assembled with MMO-40 as the cathode, $Ca(TFSI)_2$/N,N-

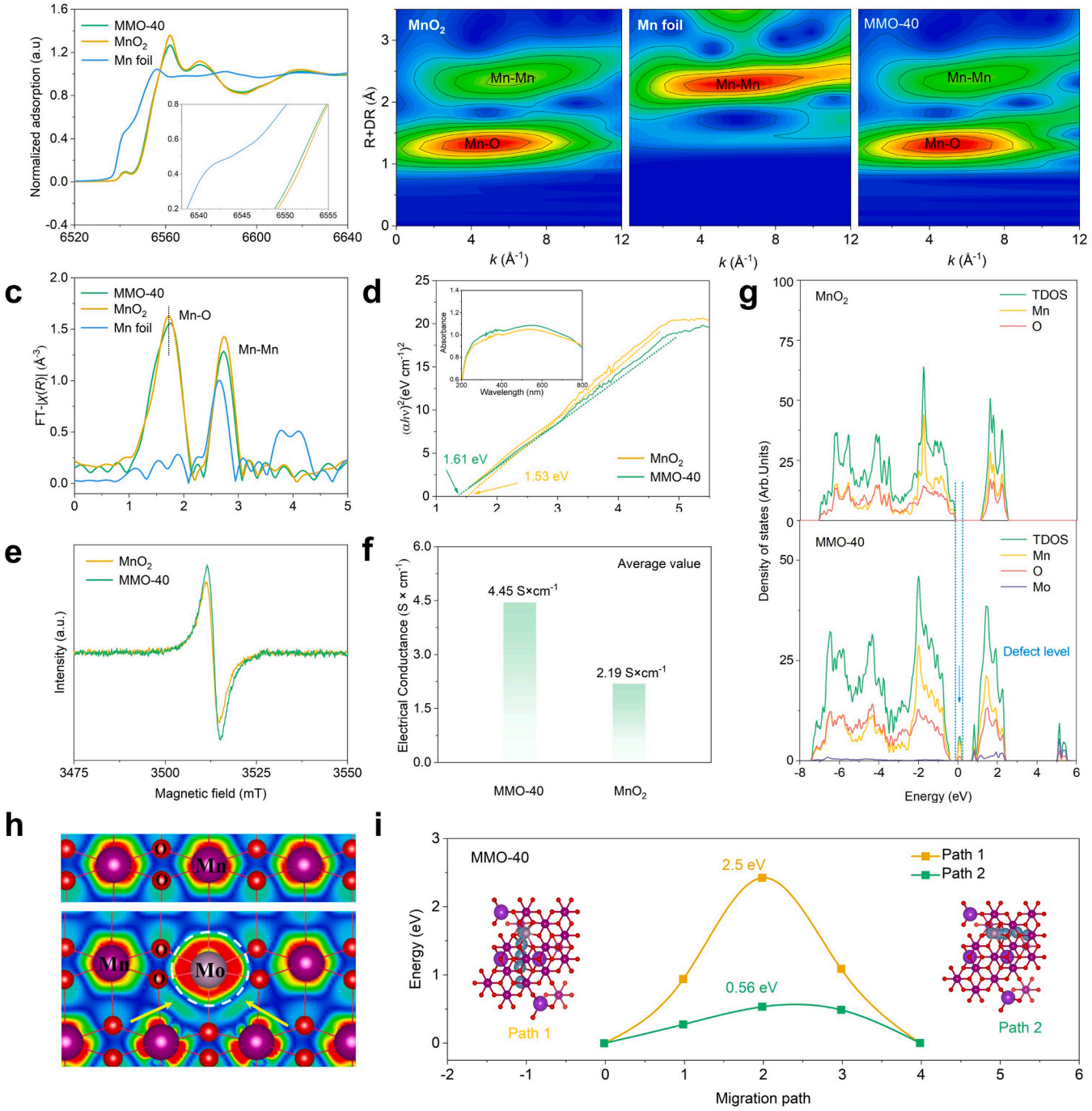

Fig. 4. (a) Normalized Mn K-edge XANES spectra of the Mn foil, MnO_2 and MMO-40. (b) Wavelet transform (WT) contour plots of Mn foil (left), MnO_2 (middle) and MMO-40 (right). (c) The radial distribution functions (RDFs) obtained from the $k^2\chi(k)$ by Fourier transform (FT). (d) Photon energy vs. $(\alpha h\nu)^2$ curves of MnO_2 and MMO-40 (inset: UV–vis diffuse reflectance spectra). (e) EPR spectra of MnO_2 and MMO-40. (f) Four points resistance of MnO_2 and MMO-40. (g) Density of states for MnO_2 and MMO-40. (h) Contour charge maps of MnO_2 and MMO-40 slabs. red and cyan regions represent the electron depletion and accumulation, respectively. (i) Ca ions migration behaviors along the a, b-axis in MMO-40.

dimethylcyclohexylamine as the electrolyte, and Ca metal as the anode. The initial discharge capacity of MMO-40 at 30 mA g^{-1} is 108 mAh g^{-1} (**Figure S14**). However, the discharge capacity of MMO-40 had decayed rapidly (**Figure S15**), which could well be due to the irreversible deposition/dissolution of Ca metal surface [31]. The electrochemical kinetics of MMO-40 were analyzed. Utilizing the multi-scan rate CV curves (Fig. 3f), the capacitive capacity contributions of MMO-40 were determined at various current densities (Fig. 3g). The capacitive capacity contribution of MMO is 72 % at the sweep rate of 0.6 mV s^{-1}, confirming that capacitive processes largely dominate the electrochemical behavior of the MMO-40 electrode (**Figure S16**). The high capacitive contribution of MMO-40 is responsible for its remarkable rate performance. Meanwhile, the galvanostatic intermittent titration technique (GITT) tests were performed on MM0-40 and MnO_2 to evaluate the Ca ions diffusion kinetics. The calculation of diffusion coefficients was derived from the GITT curves, as outlined depicted in **Figure S17**. The determined diffusion coefficients for Ca ions within the MMO-40 electrode during discharge/charge process are $2.87 \times 10^{-10} \sim 1.30 \times 10^{-11}$ and $3.61 \times 10^{-10} \sim 2.22 \times 10^{-12}$ cm^2 s^{-1} (Fig. 3h) respectively. These values surpass those of pristine MnO_2 ($3.50 \times 10^{-10} \sim 8.57 \times 10^{-14}$ and $2.54 \times 10^{-10} \sim 7.31 \times 10^{-12}$ cm^2 s^{-1}) (**Figure S18**). In addition, the resistance of MMO-40 and MnO_2 was measured by electrochemical impedence spectroscopy (EIS) (**Figure S19**). The charge transfer resistance in the MMO-40 electrode is reduced compared to pristine MnO_2, indicating enhanced interfacial charge transfer kinetics.

Further characterizations were conducted to investigate the changes in the local structure and electronic structure of Mn after Mo doping. In the XANES spectra (Fig. 4a), a weak edge front peak is present in both MnO_2 and MMO-40 compared to standard Mn, which is due to the transition of 1s electron to unoccupied 3d orbitals [53]. In order to further determine the local coordination environment of Mn atoms in MMO-40 and MnO_2, the wavelet transform (WT) technique was performed on their k-space. As shown in Fig. 4b, the bonding strength of Mn-Mn in MnO_2 is higher than that of MMO-40. This indicates that no significant structural changes have occurred, and that structural stability has been preserved. In addition, the K-edge absorption of MMO-40 is shifted to lower energies, indicating a decreased oxidation state of Mn in MMO-40 [54]. The Mn K-edge extended X-ray absorption fine structure (EXAFS) spectrum of MMO-40 exhibits a coordination structure similar to that of MnO_2 (Fig. 4c), indicating that Mo doping does not change its phase. In addition, the relative intensity of the peaks in MMO-40 is lower than that of MnO_2, indicating a decrease in the coordination number and/or an increase in the degree of disorder [53]. The UV-visible spectroscopy further reveals the impact of Mo doping in MnO_2. The MMO-40 exhibits stronger absorption in the wavelength range of 400–800 nm compared to pristine MnO_2 (Fig. 4d). Furthermore, the bandgap is reduced from 1.61 eV to 1.53 eV, indicating that Mo doping effectively enhances the intrinsic conductivity. In addition, the response of unpaired electrons in EPR spectrum is enhanced after Mo doping, confirming the increase in MMO-40 (Fig. 4e). The four-point probe experiments (Fig. 4f) indicate that the electron conductivity of the MMO-40 electrode is 4.45 S·cm^{-1}, which is significantly higher than that of MnO_2 (2.19 S·cm^{-1}). The electronic structure of MnO_2 and MMO-40 is further studied by DFT calculations. The density of states (DOS) calculated provides valid evidence for the increase in conductivity (Fig. 4g). The pristine MnO_2 exhibits a distinct band gap near the Fermi level, indicating that the pristine MnO_2 is a semiconductor with low conductivity. In contrast, due to Mo doping, a defect energy level appears at the conduction band minimum (CBM) of MMO-40, reducing the band gap and enhancing the conductivity [55].

Further, the charge density distribution of MnO_2 and MMO-40 (Fig. 4h) were analyzed using contour charge maps, in which the red and cyan regions represent electron depletion and accumulation, respectively. Compared to the Mn atoms, the red region around the Mo atoms is significantly enhanced, indicating the generation of a large number electron holes around the Mo atom. Additionally, the accumulation of electrons in the cyan region (indicated by yellow arrows in Fig. 4h) is a result of electronic redistribution after Mo doping, which further demonstrates that Mo doping enhances the charge around Mn. In addition, the Ca ions migration pathways and energy barriers of MnO_2 and MMO-40 were investigated. **Figure S20-21** illustrates the possible migration pathways of Ca ions. The calculated diffusion energy barriers for Ca ions in MMO-40 are 2.5 and 0.59 eV, respectively (Fig. 4i), whereas those for MnO_2 are 2.61 and 0.87 eV (**Figure S22**), suggesting the faster reaction kinetics of Ca ions in MMO-40. The above results demonstrate the improved electronic conductivity of the MnO_2, which shall be responsible for the improved Ca ions storage performance.

To further investigate the factors contributing to the excellent cycling performance of MMO-40, the Mn content and the material structure before and after cycling were analyzed. First, the change of the electrolyte after cycling was observed in a three-electrode system with MnO_2 or MMO-40 as the working electrode, Ag^+/AgCl as reference electrode and AC as the counter electrode. For MnO_2 as working electrode (Fig. 5a), the electrolyte undergoes a noticeable color change after 100 cycles, indicating the dissolution of Mn [12,56]. In contrast, the electrolyte for MMO-40 as working electrode remains colorless and transparent after cycling, indicating that the doping of Mo inhibits the dissolution of Mn. Moreover, the glass fiber separator in the MnO_2//AC cell exhibits a dark yellow coloration after 500 cycles, while the color change of the separator in the MMO-40//AC battery after cycling is relatively slighter (Fig. 5b). Moreover, the ICP-OES tests indicate that the Mn content of the separator in the MMO-40//AC cell is significantly lower after cycling compared to that in the MnO_2 //AC cell (Fig. 5c). To reveal the effect of J-T distortion on MnO_2, the Mn10-O bond lengths of MnO_2 and MMO-40 structures after insertion of Ca ions were compared by DFT calculation (Fig. 5d,e **and Table S4**). For MnO_2, the bond length elongation is maximized at the Mn10 site. On the contrary, the bond length variation of MnO_2 is small, improves the structural stability of MnO_2. In addition, DFT calculations were applied to evaluate the energy barriers (E) of removing Mn atom from MnO_2 and MMO-40 (Fig. 5g). An energy of 7.04 eV is required for Mn atom around Mo atom to detach from MMO-40, which is much higher than that of MnO_2 (4.86 eV). Overall, the introduction of Mo atoms effectively mitigates the J-T effect the lattice distortion, as well as inhibits the dissolution of Mn to enhance the structural stability. Furthermore, the PDF test indicate that the Mn-O bond of MMO-40 at discharged state is shorter than that of MnO_2 at discharged state (Fig. 5f), demonstrating the lattice distortion due to the J–T effect is reduced after Mo doping.

To understand the energy storage mechanism of MMO-40, both in-situ XRD and ex-situ characterization were conducted to elucidate alterations in chemical composition and crystal structure during the (de) intercalation process of Ca ions. Fig. 6a shows the diffraction peaks at 25.8° and 36.5° gradually decrease in intensity during the discharge process, suggesting that MMO-40 becomes partially disordered during the intercalation of Ca ions. In contrast, These diffraction peaks exhibited reversible recovery and gradual enhancement upon the extraction of Ca ions. The peak at 36.5° shifted slightly to a lower angle after discharge in the ex-situ XRD patterns, indicating the lattice expansion due to the insertion of Ca ions (Fig. 6b). Conversely, the peak returned to the initial position after charging, indicating lattice contraction due to the extraction of Ca ions. These findings indicate that the Ca ion storage mechanism of MMO-40 involves a reversible ordered-disordered transition. The STEM-EDS mapping images (Fig. 6c) of the discharged MMO-40 exhibit distinct profiles of Mn, O, Mo and Ca element, demonstrating the insertion of Ca ions. For MMO-40 at the charged state, the signal of Ca becomes weaker, indicating the extraction of Ca ions. The HRTEM images (Fig. 6d, e) reveal the emergence of a partially disordered structure in the discharged, while the layers are smooth after the charging process. This result suggests a transition from ordered to disordered insertion/extraction mechanism of Ca ions for MMO-40. The XPS was utilized to investigate the valence changes of Mn

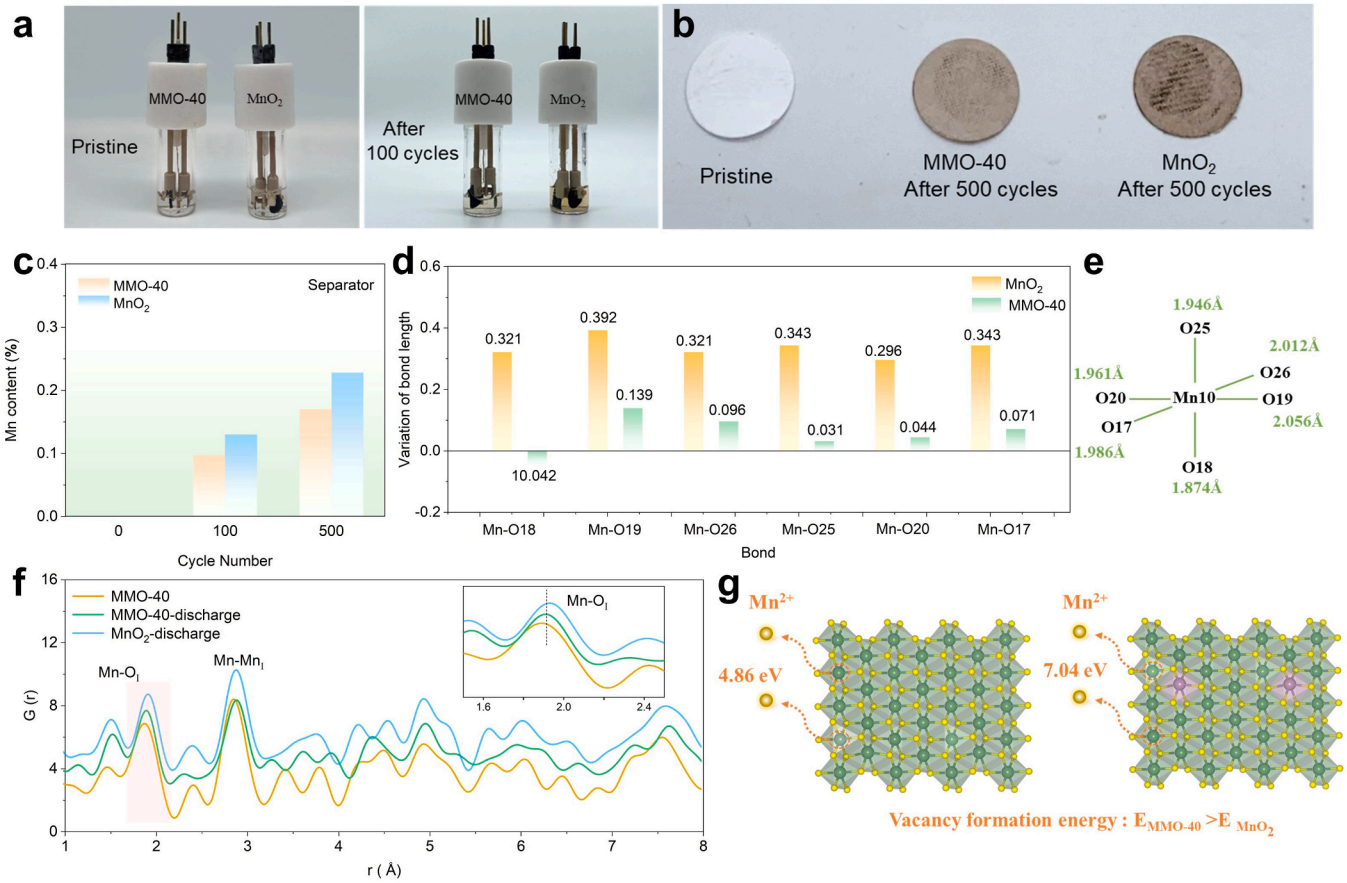

Fig. 5. Digital images of electrolyte: (a) Pristine (left) and (b) after 100 cycles. (b) Digital images of glass fiber separators: pristine state (left), after 500 cycles in AC// MMO-40 coin cell (middle) and after 500 cycles in AC//MnO_2 coin cell (right). (c) The ICP result of the glass fiber separator under different cycle number. (d,e) The variation of Mn-O bond length at discharged state for MnO_2 and MMO-40. (f) The PDF spectra in the first cycle (pristine, first charge to -1.5 V). (g) Energy barrier of manganese vacancy formation from the structure of MnO_2 and MMO-40.

during the insertion/extraction process of Ca ions. In the Mn 2p XPS spectra (Fig. 6f), the peaks at 640.4, 641.6 and 642.6 eV are associated with Mn^{2+}, Mn^{3+} and Mn^{4+}, respectively. In the discharge state, the area of the Mn^{3+} peak increased, indicating that the insertion of Ca ions caused the reduction of Mn^{4+} to Mn^{3+}. In the charge state, the recovery of Mn^{3+} peak area indicates that the change of Mn valence state is reversible during the charging/discharging process. In addition, the Ca 2p signal is observed in the discharged state and notably diminished in the charged state (Fig. 6g). Furthermore, the Ca content of MMO-40 at different states was determined by ICP tests (**Table S5**).

For MMO-40 at pristine, discharged, charged, and 2nd discharged states, the atomic ratios of Ca to Mn are 0.02:1.00, 0.10:1.00, 0.03:1.00, and 0.11:1.00, respectively. These results indicate the reversible insertion/extraction of Ca ions in MMO-40. In addition, TOF-SIMS results show that the Ca ions are inserted within the electrode of the material rather than attached to the surface (Fig. 6h, i). In the pristine state, the elements Mn and O were shown to uniformly distribute within the MMO-40 electrode, however, no obvious Ca signal is detected. In the fully discharged state, the elements Mn, O and Ca were uniformly distributed within the MMO-40 electrode, demonstrating the intercalation of Ca ions.

3. Conclusions

In summary, Mo substitutionally doped MnO_2 was successfully synthesized and assessed as cathode materials for CIBs. The doping of Mo optimizes the electronic structure and enhances the electrical conductivity of MnO_2. Meanwhile, Mo doping reduces the J-T distortion and suppresses the dissolution of Mn. The kinetic analysis and DFT results indicate that Mo doping enhances ion transport kinetics and mitigates the dissolution of Mn. Consequently, MMO-40 demonstrates remarkable rate performance (112 mAh g^{-1} at 1 A g^{-1}) and robust long cycle stability (~93.9 % capacity retention after 900 cycles at 1 A g^{-1}). Importantly, the capacity and voltage of MMO-40 are also superior to most reported cathode materials of the CIBs. This work presents a high-performance cathode materials for CIBs and provides a new insight for the development of manganese-based cathode materials.

CRediT authorship contribution statement

Chunli Zuo: Methodology, Investigation, Formal analysis, Data curation, Conceptualization. **Fangyu Xiong:** Methodology, Investigation, Conceptualization. **Yihan Shao:** Supervision, Software. **Ming Li:** Project administration, Methodology, Conceptualization. **Dongyao Zhu:** Formal analysis, Data curation. **Jiexin Zhu:** Investigation, Formal analysis. **John Wang:** Writing – review & editing, Writing – original draft, Funding acquisition. **Qinyou An:** Writing – review & editing, Writing – original draft, Project administration, Methodology, Funding acquisition.

Declaration of competing interest

The authors declare that they have no known competing financial interests or personal relationships that could have appeared to influence the work reported in this paper.

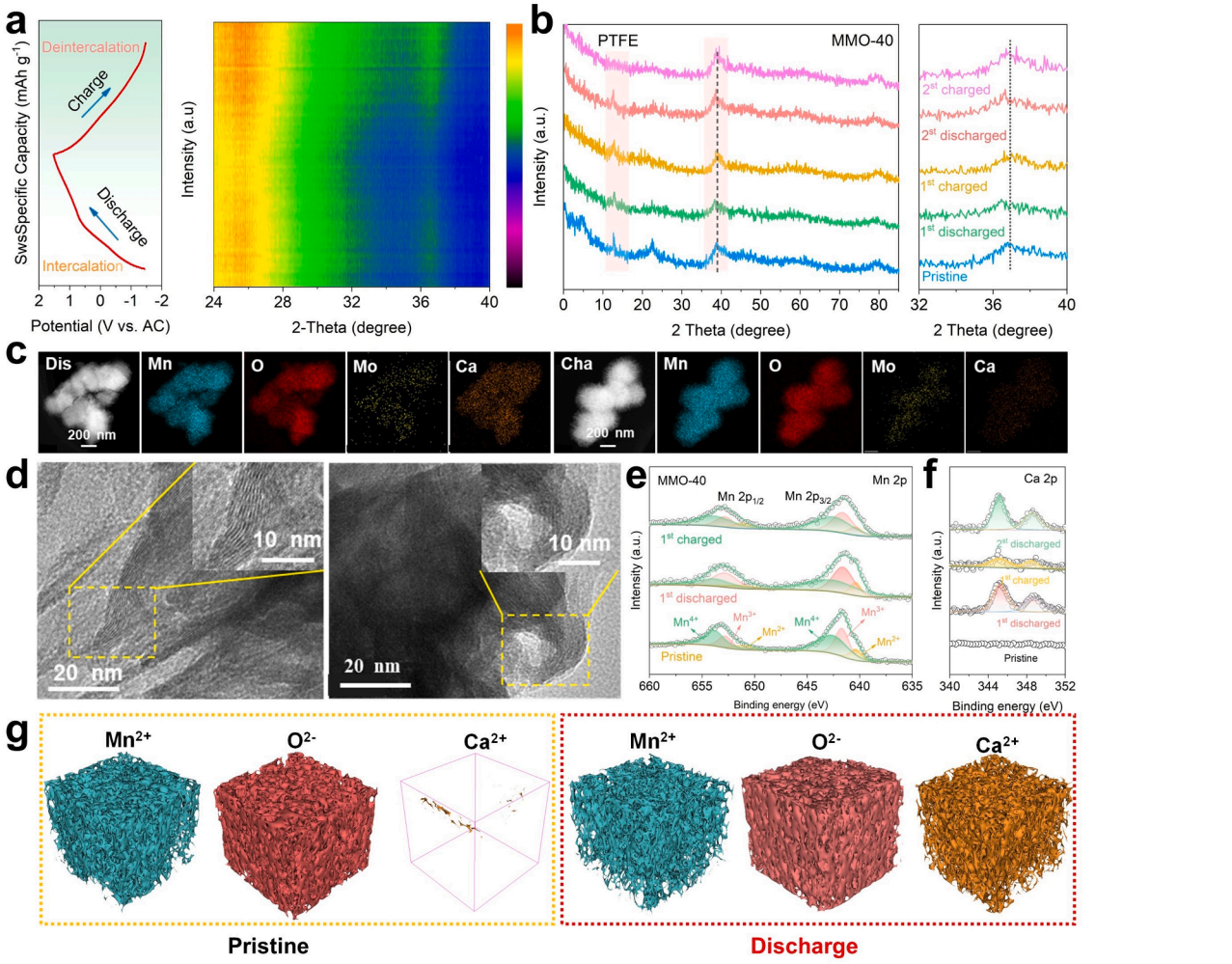

Fig. 6. (a) In-situ XRD patterns and the GCD profiles of MMO-40. (b) Ex-situ XRD of MMO-40 at different states. (c) STEM-EDS mapping images of the fully discharged and charged MMO-40 electrodes. (d,e) HRTEM images of MMO-40 at the discharged and charged states. (f,g) Mn 2p XPS spectra and Ca 2p XPS spectra of MMO-40 at different states. (h,i) TOF-SIMS 3D rendering models for the pritine and discharged MMO-40 electrode.

Data availability

Data will be made available on request.

Acknowledgements

Thanks to Prof. Liqiang Mai for their guidance in this study. This work was supported by the National Natural Science Foundation of China (52172231), the Natural Science Foundation of Hubei Province (2022CFA087), National Energy-Saving and Low-Carbon Materials Production and Application Demonstration Platform Program (TC220H06N). Chunli Zuo thanked the funding support from China Scholarship Council/ National University of Singapore for the joint Ph. D. scholarship (CSC NO.202306950114).

Supplementary materials

Supplementary material associated with this article can be found, in the online version, at doi:10.1016/j.ensm.2024.103763.

References

[1] W. Zhang, J. Liu, W. Cai, M. Zhou, W. Zhong, G. Xiao, P. Luo, Y. Zhao, Q. An, Chem. Eng. J. 464 (2023) 142711.
[2] P. Luo, W. Zhang, W. Cai, Z. Huang, G. Liu, C. Liu, S. Wang, F. Chen, L. Xia, Y. Zhao, Nano Res. 16 (2023) 503–512.
[3] M. Li, X. Wang, J. Meng, C. Zuo, B. Wu, C. Li, W. Sun, L. Mai, Adv. Mater. 36 (2024) 2308628.
[4] M. Wang, C. Jiang, S. Zhang, X. Song, Y. Tang, H.-M. Cheng, Nat. Chem. 10 (2018) 667–672.
[5] S. Kim, L. Yin, S.-M. Bak, T.T. Fister, H. Park, P. Parajuli, J. Gim, Z. Yang, R.F. Klie, P. Zapol, Y. Du, S.H. Lapidus, J.T. Vaughey, Nano Lett. 22 (2022) 2228–2235.
[6] K.V. Nielson, T.L. Liu, Angew. Chem. Int. Ed. 59 (2020) 3368–3370.
[7] H. Song, C. Wang, Adv. Energy Sustain. Res. 3 (2022) 2100192.
[8] B. Ji, H. He, W. Yao, Y. Tang, Adv. Mater. 33 (2021) 2005501.
[9] B.J. Kwon, L. Yin, C.J. Bartel, K. Kumar, P. Parajuli, J. Gim, S. Kim, Y.A. Wu, R. F. Klie, S.H. Lapidus, Chem. Mater. 34 (2022) 836–846.
[10] A. Zhang, R. Zhao, Y. Wang, J. Yang, C. Wu, Y. Bai, Energy Environ. Sci. 16 (2023) 3240–3301.
[11] Y. Zhao, R. Zhou, Z. Song, X. Zhang, T. Zhang, A. Zhou, F. Wu, R. Chen, L. Li, Angew. Chem. Int. Ed. 61 (2022) e202212231.
[12] C. Zuo, F. Xiong, J. Wang, Y. An, L. Zhang, Q. An, Adv. Funct. Mater. 32 (2022) 2202975.
[13] H. Zhang, Q. Liu, J. Wang, K. Chen, D. Xue, J. Liu, X. Lu, J. Mater. Chem. A 7 (2019) 22079–22083.
[14] H. Jang, S. Suzuki, M. Miyayama, J. Eur. Ceram. Soc. 34 (2014) 4297–4304.
[15] Y. Zhao, C. Han, J. Yang, J. Su, X. Xu, S. Li, L. Xu, R. Fang, H. Jiang, X. Zou, Nano Lett. 15 (2015) 2180–2185.
[16] J. Wang, J.-G. Wang, H. Liu, C. Wei, F. Kang, J. Mater. Chem. A 7 (2019) 13727–13735.
[17] J. Peng, Y. Li, Z. Chen, G. Liang, S. Hu, T. Zhou, F. Zheng, Q. Pan, H. Wang, Q. Li, ACS Nano 15 (2021) 11607–11618.
[18] Q. Liu, Z. Hu, M. Chen, C. Zou, H. Jin, S. Wang, S.L. Chou, S.X. Dou, Small 15 (2019) 1805381.
[19] F. Xiong, S. Tan, X. Yao, Q. An, L. Mai, Mater. Today 45 (2021) 169–190.
[20] B. Lan, Y. Xiang, X. Luo, D. Wu, L. Zhang, J. Duan, M. Guo, Y. Ito, Y. Liu, Chem. Eng. J. 430 (2022) 132886.

[21] L. Mu, R. Zhang, W.H. Kan, Y. Zhang, L. Li, C. Kuai, B. Zydlewski, M.M. Rahman, C.-J. Sun, S. Sainio, Chem. Mater. 31 (2019) 9769–9776.
[22] Y. Huang, Z. Yan, W. Luo, Z. Hu, G. Liu, L. Zhang, X. Yang, M. Ou, W. Liu, L. Huang, Energy Storage Mater. 29 (2020) 182–189.
[23] K. Chu, Y.-p. Liu, Y.-b. Li, Y.-l. Guo, Y. Tian, H.J.A.C.B.E. Zhang, 264 (2020) 118525.
[24] Y. Zhao, P. Zhang, J. Liang, X. Xia, L. Ren, L. Song, W. Liu, X. Sun, Energy Storage Mater. 47 (2022) 424–433.
[25] D. Zhang, J. Cao, X. Zhang, N. Insin, S. Wang, J. Han, Y. Zhao, J. Qin, Y. Huang, Adv. Funct. Mater. 31 (2021) 2009412.
[26] A. Xia, C. Zhao, W. Yu, Y. Han, J. Yi, G. Tan, J. Appl. Electrochem. 50 (2020) 733–744.
[27] Z. Wang, K. Han, Q. Wan, Y. Fang, X. Qu, P. Li, ACS Appl. Mater. Interfaces 15 (2023) 859–869.
[28] X. Xu, M. Duan, Y. Yue, Q. Li, X. Zhang, L. Wu, P. Wu, B. Song, L. Mai, ACS Energy Lett. 4 (2019) 1328–1335.
[29] J. Wang, S. Tan, F. Xiong, R. Yu, P. Wu, L. Cui, Q. An, Chem. Commun. (Camb) 56 (2020) 3805–3808.
[30] P.A. Chando, S. Chen, J.M. Shellhamer, E. Wall, X. Wang, R. Schuarca, M. Smeu, I. D. Hosein, Chem. Mater. 35 (2023) 8371–8381.
[31] Z.-L. Xu, J. Park, J. Wang, H. Moon, G. Yoon, J. Lim, Y.-J. Ko, S.-P. Cho, S.-Y. Lee, K. Kang, Nat. Commun. 12 (2021) 3369.
[32] C. Chen, F. Shi, S. Zhang, Y. Su, Z.L. Xu, Small 18 (2022) e2107853.
[33] B. Jeon, J.W. Heo, J. Hyoung, H.H. Kwak, D.M. Lee, S.-T. Hong, Chem. Mater. 32 (2020) 8772–8780.
[34] C. Zuo, F. Chao, M. Li, Y. Dai, J. Wang, F. Xiong, Y. Jiang, Q. An, Adv. Energy Mater. 13 (2023).
[35] J. Wang, J. Wang, Y. Jiang, F. Xiong, S. Tan, F. Qiao, J. Chen, Q. An, L. Mai, Adv. Funct. Mater. 32 (2022).
[36] J. Hyoung, J.W. Heo, B. Jeon, S.-T. Hong, J. Mater. Chem. A 9 (2021) 20776–20782.
[37] M. Adil, A. Sarkar, S. Sau, D. Muthuraj, S. Mitra, J. Power Sourc. (2022) 541.
[38] N. Ma, R. Ohtani, H.M. Le, S.R.S. SÃ¸rensen, R. Ishikawa, S. Kawata, S. Bureekaew, S. Kosasang, Y. Kawazoe, K. Ohara, Nat. Commun. 13 (2022), 2041-1723.
[39] Q. Shi, R. Qi, X. Feng, J. Wang, Y. Li, Z. Yao, X. Wang, Q. Li, X. Lu, J. Zhang, Nat. Commun. 13 (2022), 2041-1723.
[40] P. Gao, P. Metz, T. Hey, Y. Gong, D. Liu, D.D. Edwards, J.Y. Howe, R. Huang, S. T. Misture, Nat. Commun. 8 (2017), 2041-1723.
[41] M. Li, Y. Zhang, J. Hu, X. Wang, J. Zhu, C. Niu, C. Han, L. Mai, Nano Energy 100 (2022) 107539.
[42] A. Xia, C. Zhao, W. Yu, Y. Han, J. Yi, G. Tan, J. Appl. Electrochem. 50 (2020), 0021-0891X.
[43] H. Fang, H. Ji, J. Zhai, C. Wang, C. Zhu, G. Chen, M. Chu, T. Zhang, Z. Ma, W. Zhao, Small (2023) 1613–6810.
[44] W. Dong, X. Huang, Y. Jin, M. Xie, W. Zhao, F. Huang, Dalton Trans. 49 (2020) 8136–8142.
[45] Z. Zheng, Z. Tang, Z. Zhang, W. Shen, Russ. J. Electrochem. 39 (2003) 1023–1935.
[46] X. Li, Y. Xu, C. Wang, J. Alloys Compd. 479 (2009) 0925–8388.
[47] S. Tan, M. Hobday, J. Gorman, G. Amiet, C. Rix, J. Mater. Chem. 13 (2003) 1180–1185.
[48] B. Lan, Y. Xiang, X. Luo, D. Wu, L. Zhang, J. Duan, M. Guo, Y. Ito, Y. Liu, Chem. Eng. J. 430 (2022) 1385–8947.
[49] M.M. Rahman, S. McGuigan, S. Li, L. Gao, D. Hou, Z. Yang, Z. Xu, S.-J. Lee, C.-J. Sun, J. Liu, ACS Energy Lett. 6 (2021) 2380–8195.
[50] A. Zhang, X. Wang, R. Zhao, Y. Wang, J. Yue, J. Yang, C. Wu, Y. Bai, Angew. Chem. Int. Ed. (2023) 1433–7851.
[51] J. Liu, L. Yu, E. Hu, B.S. Guiton, X.-Q. Yang, K. Page, Inorg. Chem. 57 (2018) 0020–1669.
[52] A. Manceau, M.A. Marcus, S. Grangeon, Am. Mineral. 97 (2012) 1945–3027.
[53] Y. Zou, W. Zhang, N. Chen, S. Chen, W. Xu, R. Cai, C.L. Brown, D. Yang, X. Yao, ACS Nano 13 (2019) 2062–2071.
[54] S. Deng, Y. Zhang, D. Xie, L. Yang, G. Wang, X. Zheng, J. Zhu, X. Wang, Y. Yu, G. Pan, Nano Energy 58 (2019) 355–364.
[55] Z. Geng, X. Kong, W. Chen, H. Su, Y. Liu, F. Cai, G. Wang, J. Zeng, Angew. Chem. Int. Ed. 57 (2018) 6054–6059.
[56] C. Zuo, F. Chao, M. Li, Y. Dai, J. Wang, F. Xiong, Y. Jiang, Q. An, Adv. Energy Mater. 13 (2023) 2301014.